J. Fluid Mech. (1982), *vol.* 125, *pp.* 505–534
Printed in Great Britain

Turbulence and waves in a rotating tank

By E. J. HOPFINGER, F. K. BROWAND† AND Y. GAGNE
Institut de Mécanique, Université de Grenoble, Grenoble, France

(Received 11 December 1981 and in revised form 24 May 1982)

A turbulent field is produced with an oscillating grid in a deep, rotating tank. Near the grid, the Rossby number is kept large, $O(3–33)$, and the turbulence is locally unaffected by rotation. Away from the grid, the scale of the turbulence increases, the r.m.s. turbulent velocity decreases, and rotation becomes increasingly important. The flow field changes dramatically at a local Rossby number of about 0·20, and thereafter remains independent of depth. The flow consists of concentrated vortices having axes approximately parallel to the rotation axis, and extending throughout the depth of the fluid above the turbulent Ekman layer. The number of vortices per unit area is a function of the grid Rossby number. The local vorticity within cores can be a factor of 50 larger than the tank vorticity 2Ω. The total relative circulation contained in the vortices remains, however, a small fraction of the tank circulation.

The concentrated vortex cores support waves consisting of helical distortions, which travel along the axes of individual vortices. Isolated, travelling waves seem well-described by the vortex-soliton theory of Hasimoto (1972). The nonlinear waves transport mass, momentum and energy from the vigorously turbulent region near the grid to the rotation-dominated flow above. Interactions between waves, which are frequent occurrences, almost always result in a local breakdown of the vortex core, and small-scale turbulence production. Usually the portions of broken core reform within $\frac{1}{2}$–1 rotation periods, but occasionally cores are destroyed and reformed on a much longer timescale.

1. Introduction

Considering the wide range of practical application of rotating turbulent flow to geophysical and astrophysical phenomena, and also to rotating machinery, the information available is surprisingly scarce. Experiments have been performed by Gough & Lynden-Bell (1968), Bretherton & Turner (1968), Ibbetson & Tritton (1975), McEwan (1976), Colin de Verdiere (1980), and most recently Dickinson & Long (1982). These experiments cover a variety of flow regimes, and emphasize different aspects of the motion.

Gough & Lynden-Bell (1968), Bretherton & Turner (1968), and Ibbetson & Tritton (1975) were interested in demonstrating the effect of turbulent mixing upon the mean distribution of angular momentum. Scorer (1966) had earlier considered a rotating flow with axial symmetry and speculated that small-scale turbulent mixing would make the distribution of angular momentum roughly constant. This would mean that vorticity would be removed from the mixed region and concentrated at the centre and on the boundaries of the system. Neither Bretherton & Turner nor Ibbetson & Tritton were able to demonstrate significant vorticity expulsion (angular-momentum mixing).

† Permanent address: Department of Aerospace Engineering, University of Southern California, Los Angeles, CA 90007.

McEwan (1976) examined the turbulent flow more carefully, and showed that there did exist *local* accumulations of vorticity. Indeed the major feature of the flow was the presence of a number of such vortices populating the cross-section of the tank. Concentration by a factor of 2–3 times the background vorticity 2Ω was shown by McEwan. Colin de Verdiere (1980) has attempted to model a large-scale geophysical system on an f-plane and a β-plane. He used low-frequency boundary forcing, which would be appropriate for the mesoscale eddy system in the ocean. Local concentrations of vorticity were again an important feature of the flow. Dickinson & Long (1982) have studied the propagation of a turbulent front in a rotating container. They observed a change in propagation velocity and flow structure at a certain distance away from the forcing plane.

Experiments aimed at understanding turbulent flows in rotating machinery are few in number also. As examples we cite the work of Escudier (1979), Escudier & Zehnder (1982) and Escudier, Bornstein & Maxworthy (1982). For simplicity, their experiments involved no rotating parts, but did contain concentrated vorticity and turbulent breakdown as common features. The concentration of vorticity was produced by strong axial motion. The vortices underwent a complex series of transitions or vortex breakdowns, which are well described by Escudier & Zehnder (1982) and Escudier *et al.* (1982).

Most of the rotating-flow experiments to date have been performed in relatively shallow tanks (the exception is the recent experiment of Dickinson & Long, which proceeded independently). This has precluded the possibility of studying what seemed to us to be an important aspect, *the transition from strongly three-dimensional turbulence to a turbulent flow dominated by rotation.* The present experiment utilizes a deep tank, where we can be sure to capture this transition phenomena. We have also chosen to generate turbulence by means of an oscillating monoplane square-bar grid. More is known about the details of the turbulent field generated by an oscillating grid (see Hopfinger & Toly 1976) than for any of the previously used excitation methods.

The present study reveals an unexpected variety of phenomena that have not been discussed or commented upon before. Among these are the observations showing the extreme degree of vorticity concentration, and the observations of soliton propagation (Hopfinger & Browand 1982). We note also the close connection between previous studies of vortex breakdown, and our observations of vortex-core disruptions produced by the interaction of travelling solitons. Section 2 is a brief description of the apparatus, and §3 contains a discussion of results. In §4, we compare the experimental waveform with theory; and discuss wave interactions in §5. Section 6 contains a summary and a few concluding remarks.

2. Experimental apparatus

The experiments were conducted in a transparent cylindrical tank 40 cm in diameter and 80 cm in depth, shown schematically in figure 1. A turbulent velocity field was generated in this tank by means of a grid oscillating about a horizontal plane, located 15 cm above the lower endwall. By keeping the generating grid some distance away from the endwall, unwanted secondary motions are likely to be kept to a minimum, according to Hopfinger & Toly. The observed phenomena do not depend upon the position of the grid with respect to the bottom. When a false bottom was placed close to the grid (allowing for about 5 mm spacing when the grid was in the lower position) no qualitative difference in flow structure could be noticed. The grid consisted of 1 cm square bars with a mesh $M = 5$ cm. The stroke S (defined as twice

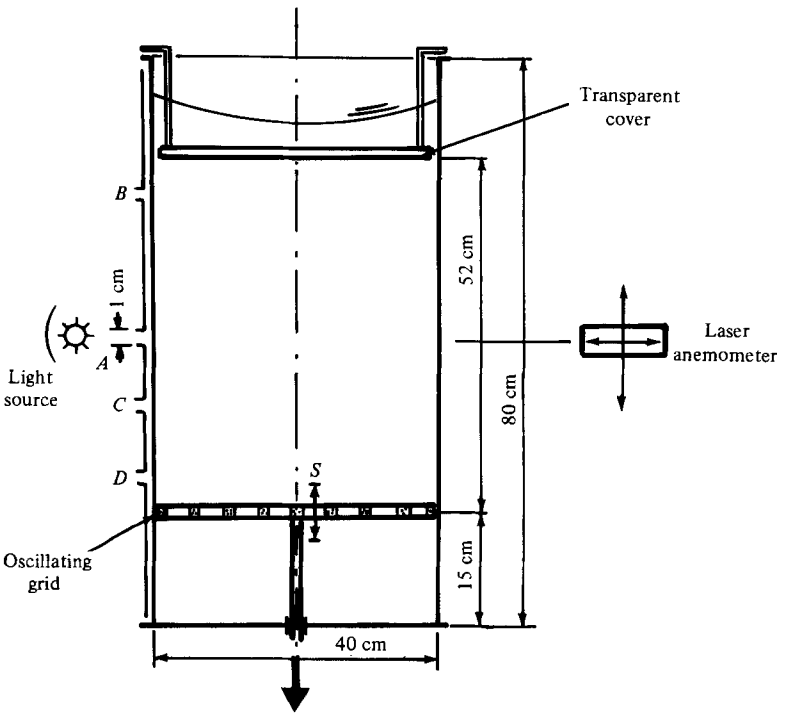

FIGURE 1. Schematic of the experimental set-up. The positions of visualisations *A*, *B*, *C*, *D* are respectively at $z = 30$ cm, 45 cm, 15·5 cm, 5·5 cm. The direction of tank rotation is clockwise.

the amplitude) and the frequency n of the grid oscillation could be adjusted over a wide range ($n \leqslant 20$ rad s^{-1}, $S \leqslant 5$ cm). The r.m.s. horizontal turbulent velocity and the integral scale in a non-rotating system were given by Hopfinger & Toley (1976) as

$$u = \frac{CnS(SM)^{\frac{1}{2}}}{z} = \frac{K_1 n}{z}, \tag{2.1}$$

$$l = K_2 z, \tag{2.2}$$

where K_1 and K_2 are functions of S for given n, and z is measured from the midplane of the oscillating grid. (Hopfinger & Toly showed that the origin determined by $l = 0$ lies slightly below the midplane, but for convenience we take $z = 0$ in the grid midplane and adjust K_1 and K_2.) For $S = 4$ cm, the value used in all the experiments, the corresponding values for the constants are $C = 0{\cdot}29/2\pi$ or $K_1 = 0{\cdot}83$ cm^2 and $K_2 = 0{\cdot}26$. The tank (including the grid) was mounted on a one metre diameter rotating table. Rotation rate could be adjusted continuously up to 2π rad s^{-1} and kept constant to well within 1 % of the rotation rate. The precision in alignment of the tank with respect to the table was better than 5 s of arc. A transparent cover was placed below the free surface in the upper end of the tank to eliminated unwanted β-effects and to improve the optical quality of the free surface (it remained free from disturbances). The cover was 52 cm above the grid midplane. Measurements were made by analysing time-exposure pictures and 16 mm ciné films. Horizontal slices of fluid approximately 1 cm thick, and containing trace amounts of wood particles (≈ 300 μm diameter), were illuminated at positions $A = 30$ cm, $B = 45{\cdot}5$ cm, $C = 15{\cdot}5$ cm and $D = 5{\cdot}5$ cm (see figure 1) to determine the flow field as a function

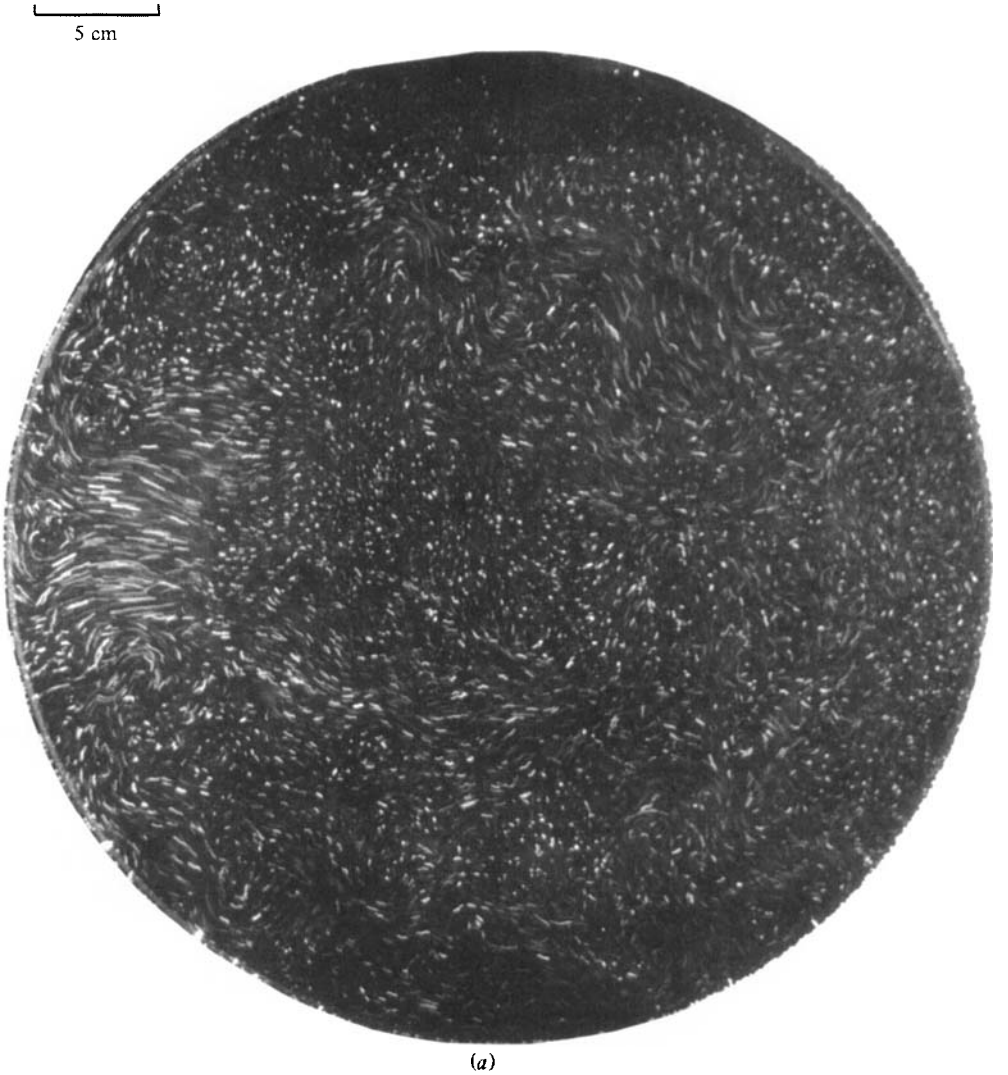

(*a*)

FIGURE 2(*a*). For caption see facing page.

of depth. Information about the flow parallel to the rotation axis was obtained by illuminating a vertical slice of approximately 2 cm thickness. Mean-flow measurements were made with a laser-Doppler anemometer.

Most of the experiments were conducted at a grid oscillation frequency of $6{\cdot}63 \times 2\pi$ rad s^{-1} and for a tank rotation rate of 2π rad s^{-1}. Some runs were made with grid frequencies of $3{\cdot}3 \times 2\pi$ and 20π rad s^{-1}, and for tank rotation rates of π, and $0{\cdot}2\pi$ rad s^{-1}. The non-dimensional parameters characterizing the flow are as follows:

$$\frac{n}{f} = 3\text{–}33, \quad \frac{ul_s}{\nu} = 10^3, \quad \frac{\nu}{fl_s^2} = 10^{-5}, \quad \frac{u}{fl_s} = 5 \times 10^{-2}, \quad \frac{H}{l_s} = 3\text{–}6.$$

Here u and l_s are, respectively the velocity and lengthscale associated with the horizontal flow field far from the grid, H is the depth of the fluid column, and $f = 2\Omega$.

(*b*)

FIGURE 2. Streakline photographs of the turbulent flow field in a cross-section of the tank 30 cm above the grid midplane, (view from above): (*a*) without rotation, $n = 13{\cdot}3\pi$ rad s^{-1}, ($S = 4$ cm); (*b*) with rotation (clockwise tank rotation as indicated by the arrow), $n = 13{\cdot}3\pi$ rad s^{-1}, $\Omega = 2\pi$ rad s^{-1} ($Ro_g = 3{\cdot}32$). The exposure time was 0·25 s.

3. Experimental results

3.1. *Vortex genesis (revealed by observations in a horizontal plane)*

The most striking effect rotation has upon turbulent field is the generation of intense vortices. This is clearly seen from a comparison of the streakline photographs shown in figure 2. This figure illustrates the instantaneous velocity field in a cross-section of the tank, located at position A (30 cm above grid midplane). Figure 2(*a*) shows the velocity field without rotation and figure 2(*b*) that with rotation. The arrow in figure 2(*b*) indicates the clockwise tank rotation. The exposure time was $\frac{1}{4}$ s. In both

cases the grid oscillation frequency was 6·63 Hz. Figure 2 (*b*) was taken in the rotating frame of reference, and shows the velocity field *relative* to rigid-body rotation at $\Omega = 2\pi$ rad s^{-1}. The velocity fluctuations near the grid are proportional to the product nS, while the magnitude of the Coriolis force is proportional to $2\Omega S$. Roughly speaking, the ratio $n/2\Omega$ is a Rossby number associated with the flow near the grid. We refer to this Rossby number as Ro_g. For the conditions shown in figure 2 (*b*), $Ro_g = 3{\cdot}32$.

With rotation, the flow field now contains a seemingly random collection of regions of coherent eddy motion. Visualizations at positions *B* (45·5 cm above grid) and *C* (15·5 cm) showed a similar result, but at *D* (5·5 cm) the presence of coherent eddies became less evident. Careful observation of video films indicated a sense of rotation that is principally cyclonic (same direction as tank rotation). Thus the motions cannot be inertial waves (which must be anticyclonic), but rather represent local areas of increased vorticity, which we will simply call vortices. Vortices have also been observed by McEwan (1976), and there is some indication of vortices in the experiment by Dickinson & Long (1982). The velocity field in the vicinity of typical vortex cores (for $Ro_g = 3{\cdot}32$) is roughly 6–10 cm/s at a radius of 1 cm. It is very difficult to obtain reliable velocity information from these observations of tracer-particle trajectories. The major problem is the ambiguity in defining the beginning and end of individual particle paths. (Particles having a vertical velocity component can pass in or out of the light during the exposure time.) It is, however, noteworthy that the vortex cores generally contain few tracer particles. We attribute this fact to the centrifuging of the heavier wood particles (particle density $\approx 1{\cdot}15$ g/cm^3). Absence of particles in the cyclonic cores suggests that larger velocities may exist there.

If the turbulence intensity at the grid is increased by increasing the oscillation frequency, or if the rotation rate is decreased for fixed oscillation frequency, then anticyclonic vortices (relative to the rotating frame) are also observed. Examples are shown in figure 3 (*a*) for a Rossby number $Ro_g = 6{\cdot}63$, and in figure 3 (*b*) corresponding to $Ro_g = 33{\cdot}2$. These photographs were taken at the same position as those shown in figure 2, but with the exposure time increased to 0·5 s. The outer arrows in figures 3 (*a*, *b*) indicate the clockwise tank rotation, and the arrows drawn inside the tank boundary indicate the existence of cyclonic (here clockwise) and anticyclonic vortices, as was observed by means of a video camera. At a Rossby number of 6·6 the anticyclonic vortices are not scattered randomly, but occupy a ring of fluid near the outer boundary. These vortices have much higher particle concentrations in the core regions, which suggests that they are much less intense than their cyclonic counterparts. For the largest Rossby number, $Ro_g = 33{\cdot}2$, anticyclonic and cyclonic vortices are, perhaps, more interspersed.

The presence of intense cyclonic vortices and (much) weaker anticyclonic vortices can be understood in simplest terms as a local stretching of the basic axial (rigid-body) vorticity field. That is, vertical stretching and (horizontal convergence) can produce local *increases in vorticity that are many times the background vorticity* 2Ω. However, local horizontal divergence can only deplete the background vorticity to produce anticyclones of strength, -2Ω.

The total population of vortices decreases with increasing Rossby number, and their size and average spacing increase. In figure 4 we have plotted the number N, of vortices, as a function of inverse Rossby number $1/Ro_g$. The error bars on N are large because the selection criterion for vortices is somewhat subjective. Even so, figure 4 suggests a linear dependence between the number of vortices and the inverse

grid Rossby number $1/Ro_g$, except perhaps for the largest value of Ro_g. A linear relation between the number of vortices and the inverse grid Rossby number would be supported by the assumption that a transition from three-dimensional turbulence to a turbulent flow dominated by rotation takes place at a certain height above the grid and represents a *fixed* value of Rossby number based on *local* flow properties. This result (which will be developed in §3.3) implies

$$N \approx KRo_T\left[\frac{1}{Rl_g}\right], \tag{3.1}$$

where K is a constant and Ro_T is the Rossby number characteristic of the transition to rotation-dominated turbulence.

Video film observations at $Ro_g = 3{\cdot}32$ show the vortices to be clearly present over times of at least 7–10 s, and occasionally even longer. During this time, the individual vortex strengths vary quasi-periodically until, and at some stage, the vortices lose coherence and become unrecognizable. The typical lifetimes are much longer than any eddy turnover time. It is not clear from these observations whether individual vortices are created and destroyed on this timescale or whether the vortices exist more or less permanently, but have highly modulated core strengths. Arguments in favour of destruction are, however, developed in §5.

3.2. *Expulsion of mean vorticity*

When the grid Rossby number is small, the mean flow is nearly solid-body rotation, but for larger grid Rossby numbers, significant departures from constant vorticity (solid-body rotation) are observed. These conclusions can be obtained directly from the previous figures. For example, contrast figure 2(*b*) with figure 3(*a*), where the mean drift is clearly indicated near the wall. In figure 3(*b*) the mean flow meanders considerably, but still exists. The qualitative result is born out by laser-anemometer measurements of the mean flow. The measured values of velocity are plotted in figure 5 as the corresponding mean vorticity, normalized by 2Ω, for $Ro_g = 3{\cdot}32$, $6{\cdot}63$ and $33{\cdot}2$. The integral of the vorticity distribution for the two lower values of Ro_g gives a constant value for the total circulation, and this serves as a convenient check on the measurements. For $Ro_g = 33$, the region near the centre is not accessible, and no integration was made.

At $Ro_g = 3{\cdot}32$, the vorticity is nearly equal to 2Ω everywhere, although there exists a slight excess (increased rotation) near the centre, and a slight counter-current (decreased rotation) near the outer boundary. As the Rossby number is increased, a substantial decrease in local mean vorticity develops, which is coincident with a strong counter-current. In the words of previous researchers, an 'expulsion' of vorticity takes place from the intermediate region to the region nearer the outer wall and to the region nearest the centre. The deficit in vorticity when $Ro_g = 6{\cdot}63$ coincides with the centres of the anticyclones located near the boundary in figure 3(*a*). The size of these anticyclones is roughly equal to the extent of the vorticity-defect region in figure 5. At the highest value of Ro_g the distribution of mean vorticity again changes shape. The low-vorticity region broadens and shifts to smaller radius, although the minimum vorticity remains approximately $\frac{1}{2}$ (2Ω). More vorticity is collected near the centre of rotation and less is collected near the outer wall.

3.3. *Transition to rotation-dominated turbulence*

In §3.1. it was mentioned that a linear relation between number of vortices and inverse grid Rossby number is consistent with a transition in flow structure that occurs at

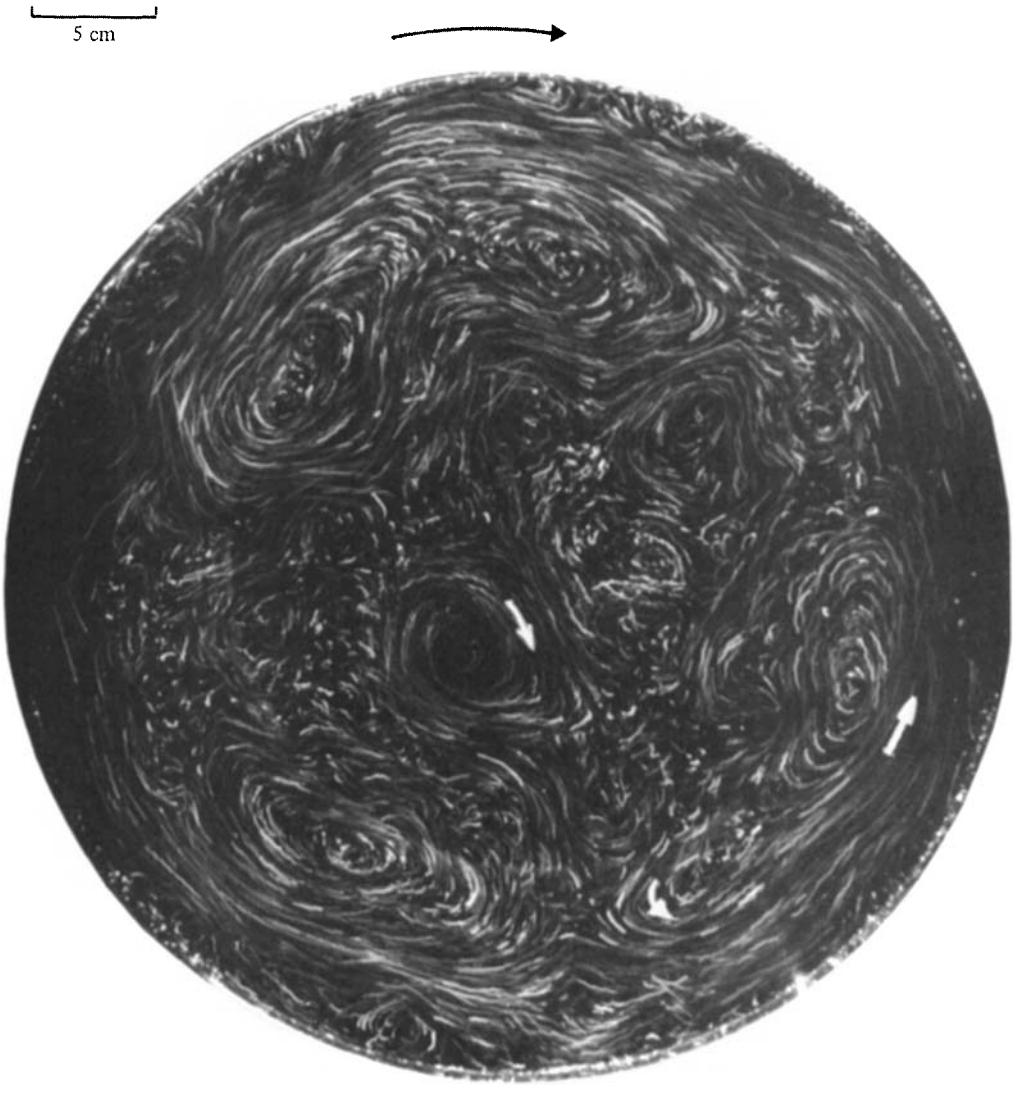

FIGURE 3(*a*). For caption see facing page.

a fixed value of local Rossby number. The reasoning will now be developed, and additional experimental evidence provided for support. First, it is clear that such a transition *must* take place somewhere in the depth of the tank, because the flow near the grid (Rossby numbers are large) is unaffected by rotation, and the flow far away is dominated by rotation. It is known from the experiments of Hopfinger & Toly (1976) (see (2.1)) that in the three-dimensional regime velocity fluctuations must decrease with distance away from the grid (z in our case), and that scales of turbulence must increase. Thus a local Rossby number, defined as

$$Ro = \frac{u(z)}{2\Omega\, l(z)},$$

will decrease with distance from the grid. The evidence is that a transition in flow

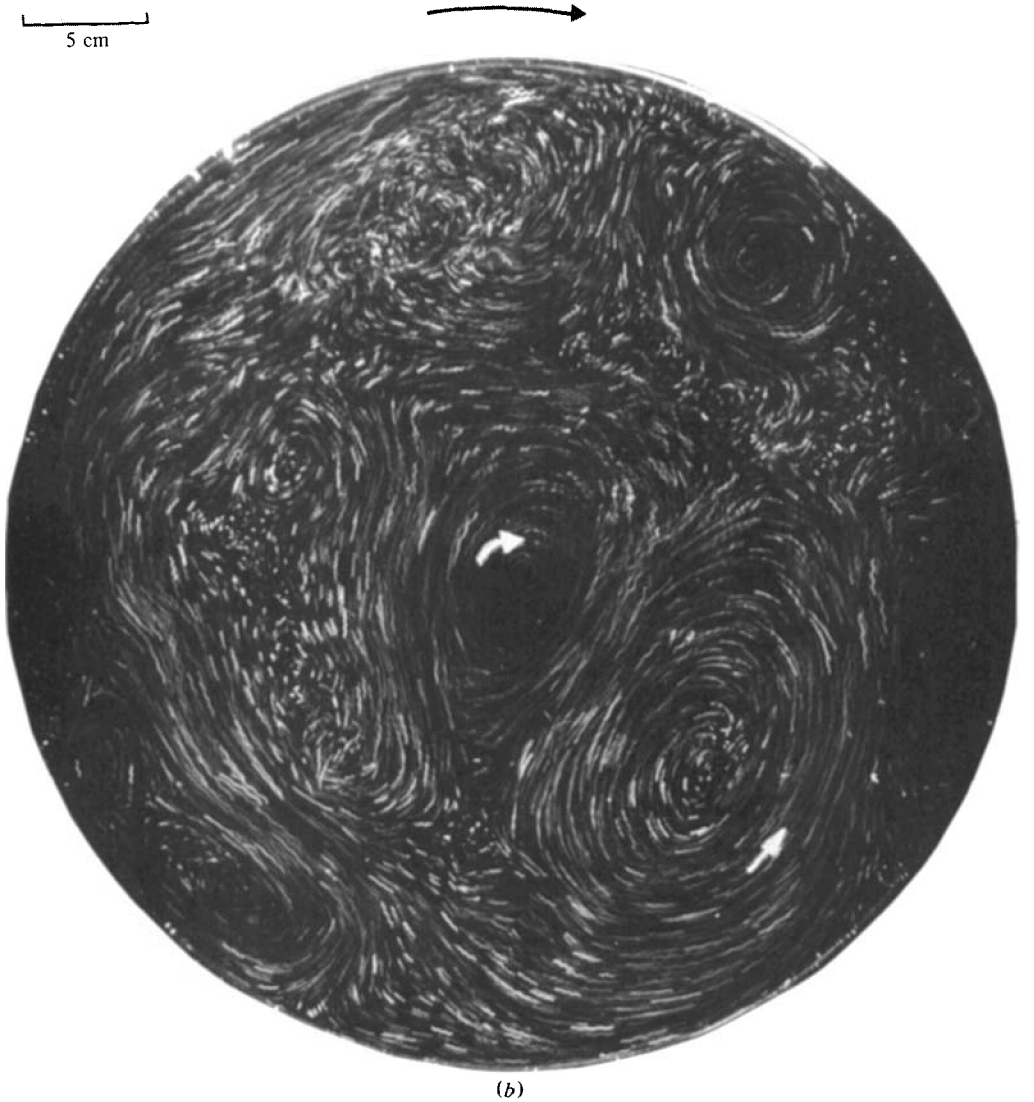

(*b*)

FIGURE 3. Streakline photographs of the turbulent flow field in a cross-section at $z = 30$ cm for $n = 13{\cdot}3\pi$ rad s^{-1} (view from above, clockwise tank rotation indicated by dark arrow): (*a*) $\Omega = \pi$ rad s^{-1} ($Ro_g = 6{\cdot}63$); (*b*) $\Omega = 0{\cdot}2\pi$ rad s^{-1} ($Ro_g = 33{\cdot}2$). Exposure time 0·5 s. The arrows inside the tank boundary are added to indicate cyclonic (clockwise) and anticyclonic (counter-clockwise) vortices.

structure occurs rather abruptly. The change in mean azimuthal velocity relative to the rotating frame with height z normalized by mesh size M, is shown in figure 6 for three grid Rossby numbers. The measurements were made at $r/R = 0{\cdot}9$ ($r/R = 0{\cdot}8$ for $Ro_g = 33{\cdot}2$), and show roughly similar behaviour for the two lower Rossby number cases. In the region nearest the grid the mean flow relative to the rotating frame is anticyclonic but small. As distance from the grid increases, the mean anticyclonic motion increases, overshoots and then approaches an asymptotic value, which remains unchanged with further increase in z. At the largest grid Rossby number the mean flow nearer the grid is cyclonic, then becomes anticyclonic, as it approaches

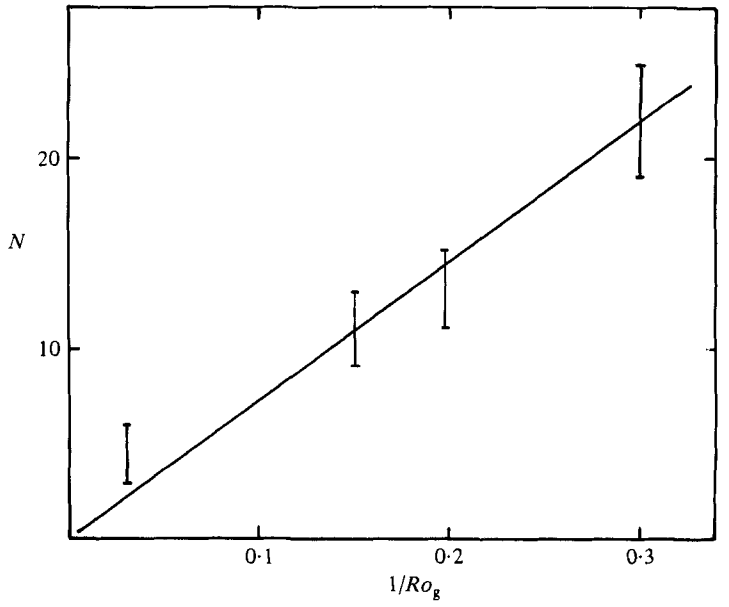

FIGURE 4. Number of vortices in a cross-section plotted as a function of inverse grid Rossby number. The straight line expresses the linear dependence given by (3.6).

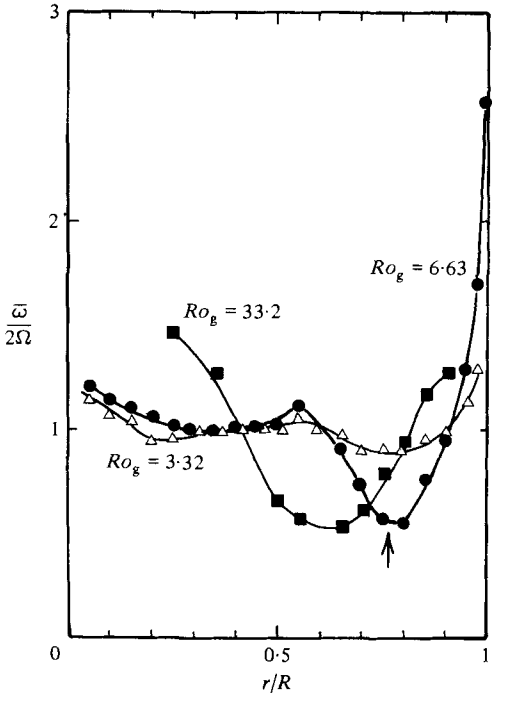

FIGURE 5. Mean absolute vorticity normalized by 2Ω as a function of tank radius: △, $Ro_g = 3{\cdot}32$; ●, 6·63; ■, 33·2. The arrow indicates the position of the anticyclonic vortices when $Ro_g = 6{\cdot}63$.

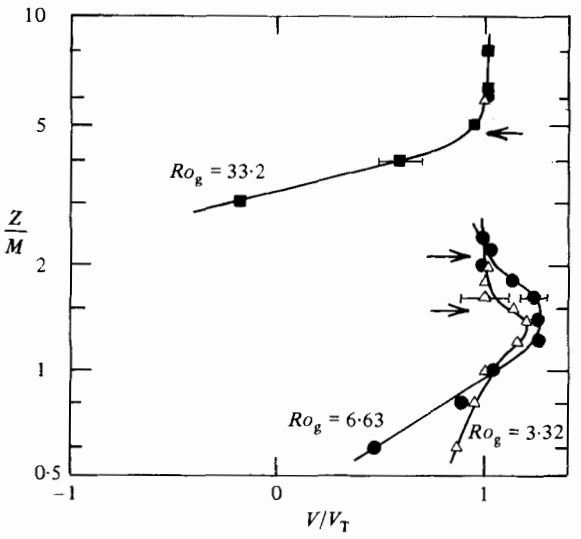

FIGURE 6. Mean velocity in a rotational frame as function of z/M measured at $r/R = 0{\cdot}9$ for $Ro_g = 3{\cdot}32$ and $6{\cdot}63$, and at $r/R = 0{\cdot}8$ for $Ro_g = 33{\cdot}2$: △, $Ro_g = 3{\cdot}32$, $v_T/\Omega R_{tank} = -0{\cdot}019$; ●, $6{\cdot}63$, $-0{\cdot}105$; ■, $33{\cdot}2$, $-0{\cdot}114$. v_T represents the largest departure (far above the grid) from the state of rigid-body rotation. The arrows mark the position of transition in flow regime.

the asymptotic value (at $r/R = 0{\cdot}8$). The heavy arrows in the figure mark the beginning of the region in each case, where azimuthal velocity becomes independent of the vertical coordinate. Visual observations above and below this point (at 15·5 cm and 5·5 cm for $Ro_g = 3{\cdot}32$ and $6{\cdot}63$) confirm the qualitative difference in flow structure, i.e. the flow nearer the grid lacks the organized vortices seen in previous photographs. Thus the position of the arrows marks the onset of rotation-dominated turbulence.

The consequences of assuming an abrupt transition at a fixed local Rossby number are as follows. Assume that near the grid

$$u(z) = \frac{K_1 n}{z}, \tag{3.2}$$

$$l(z) = K_2 z, \tag{3.3}$$

where u is fluctuation level; l is integral scale; z is distance from grid, and K_1, K_2 are constants (see (2.1), (2.2)). This should apply up to the point of transition. Setting

$$Ro = Ro_T = \text{constant} = \frac{u(z_T)}{2\Omega\, l(z_T)},$$

and substituting (3.2) and (3.3) gives an expression for Ro_T in terms of the transition distance z_T:

$$Ro_T = \frac{K_1}{K_2}\frac{n}{2\Omega}\frac{1}{{z_T}^2}.$$

Using values of K_1 and K_2 given in §2 with the three transition distances observed at the three grid Rossby numbers yields the value

$$Ro_T \approx 0{\cdot}20.$$

This result can be used to write a general expression for the turbulent Ekman-layer thickness, by defining the Ekman-layer thickness to be the transition distance z_T. Thus

$$\delta \equiv z_T = \left[\frac{K_1}{K_2}\frac{1}{Ro_T}\frac{n}{2\Omega}\right]^{\frac{1}{2}}, \tag{3.4a}$$

which becomes

$$\delta \approx 4{\cdot}0\left(\frac{n}{2\Omega}\right)^{\frac{1}{2}} \quad \text{(cm)}. \tag{3.4b}$$

Dickinson & Long (1982) observe a similar transition in flow structure. Their value for the transition Rossby number, based on visualizations is, in our terminology, 0·27–0·31.

The scale of the eddies first affected by rotation is approximately

$$l_T \approx K_2 z_T = \left[\frac{K_1 K_2}{Ro_T}\frac{n}{2\Omega}\right]^{\frac{1}{2}}, \tag{3.5a}$$

giving

$$l_T \approx 1{\cdot}03\left(\frac{n}{2\Omega}\right)^{\frac{1}{2}} \quad \text{(cm)}. \tag{3.5b}$$

For a grid Rossby number of 3·32, this results in an eddy size of the order of 1·9 cm, which is approximately the scale of the active regions seen in figure 2(*b*). For a grid Rossby number of 33·2 the prediction is 5·8 cm, which is also in rough agreement with figure 3(*b*).

If the spacing of vortices is used as the typical scale, and it is assumed that the spacing is some multiple of the transition distance,

$$\text{spacing} = l_s \sim l_T \sim z_T,$$

then the previous expression (3.1) for the number of vortices in the cross section follows immediately:

$$N = \frac{\text{area of tank}}{\text{area of vortex}} \approx \frac{D^2}{l_s^2} = K\,Ro_T\frac{1}{Ro_g}, \tag{3.6}$$

where D is the tank diameter. The value of K determined from the slope in figure 4 gives a value for the ratio of vortex-spacing/vortex-size of $l_s/l_T = 4{\cdot}5$, which again is in accord with the visual observations. Finally, a Rossby number for the turbulence, based on vortex spacing, is $Ro_s = 0{\cdot}20/4{\cdot}5 = 0{\cdot}044$, and this is comparable to Rossby numbers estimated by Colin de Verdiere (1980) for a similar experiment, but using low-frequency (low-Rossby-number) forcing.

3.4. *Vortex strength (observation in a vertical plane)*

The photographs discussed earlier have suggested that vorticity is highly concentrated in cores of relative small extent. In order to visualize these vortex regions, we have illuminated a vertical slice of approximately 2 cm width through the centre of the tank. Tiny gas bubbles are introduced into the bottom of the tank, and these collect in the low-pressure vortex cores to provide a means of visualization. Such a vortex-core visualization is shown in figure 7 for a Rossby number $Ro_g = 3{\cdot}32$. The result is surprising! The cores are extremely thin – the one in figure 7 is typical – and extend, coherently, over the entire depth of the flow. Generally speaking, cores are aligned with the rotation axis, but, of course, they are not precisely vertical. They undergo large-scale distortions, presumably produced by neighbouring cores, and appear to

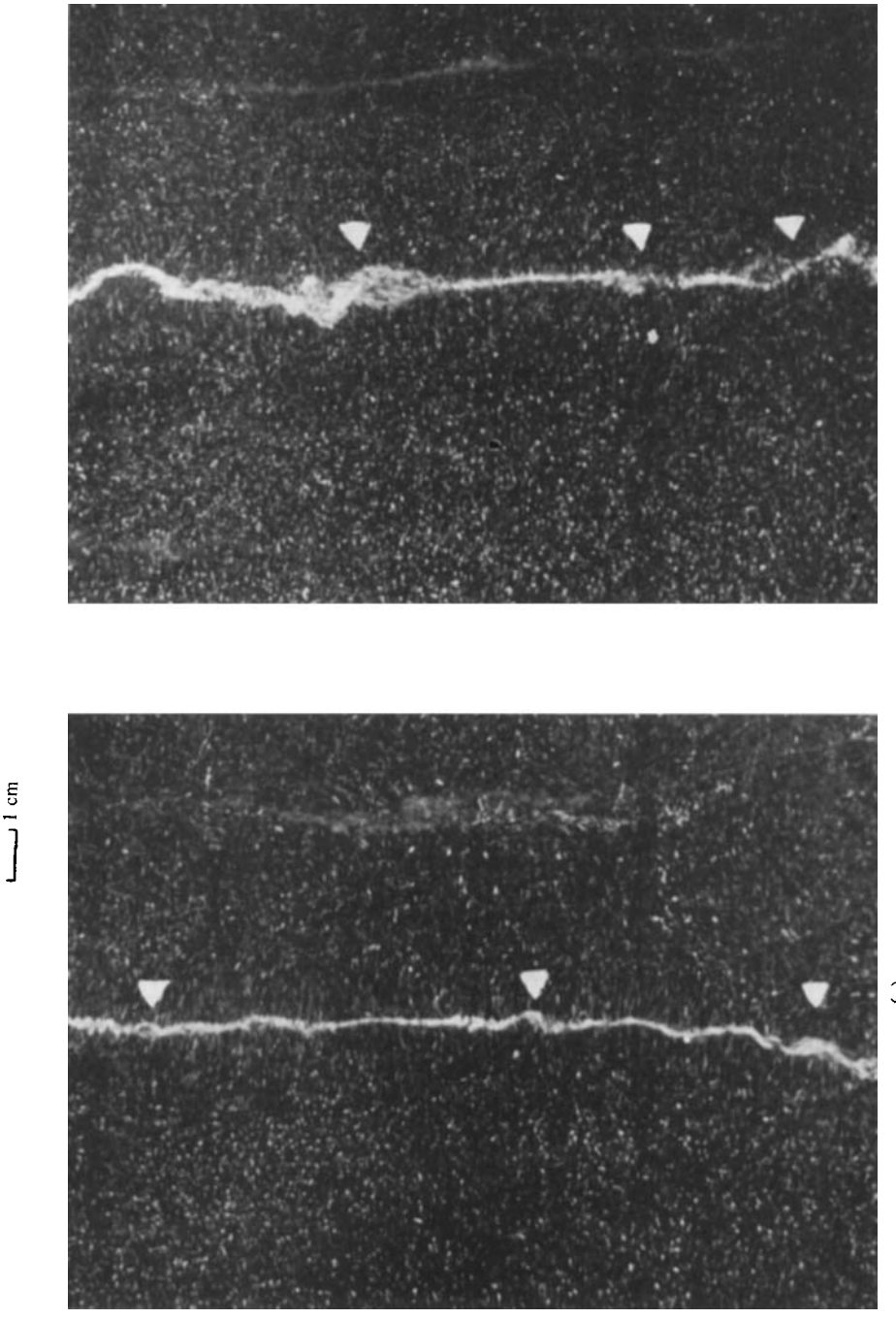

FIGURE 7. Photographs of a vortex core made visible by small air bubbles introduced into the tank ($Ro_g = 3{\cdot}32$). Between (*a*) and (*b*) 2 s have elapsed. The arrows mark wave disturbances on the core.

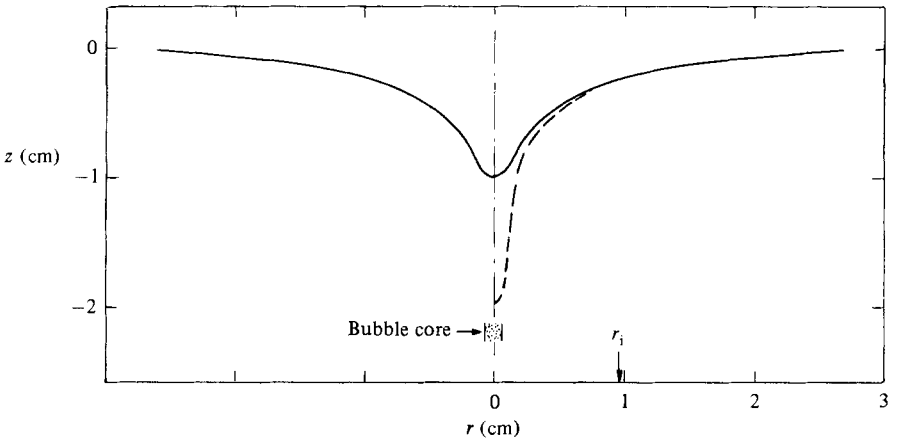

FIGURE 8. Free-surface deformations produced by a vortex ($Ro_g = 3{\cdot}32$): ——, observed; – – – –, corrected for surface tension. The radius $r_i = (\Gamma/2\pi\Omega)^{\frac{1}{2}}$.

wander slowly about the tank. There are also many smaller-scale distortions (several are marked in figure 7), which propagate along the core. (These disturbances are discussed in §§3.5 and 4.) One might describe such a flow field as being quasi-two-dimensional, that is having significant – but not perfect – correlation in the vertical direction.

Visual estimates of the illuminated core diameters give a number like 1–2 mm. The relation between the vortex core and the illuminated core size is uncertain, and another method was used to estimate the actual distribution of vorticity. The cover was removed from the tank and the water level lowered to about 30 cm (for photographic reasons). The free surface was now populated with tiny craters, each one reflecting a concentrated vortex below. By filming the cross-section of such craters (correcting for distortion through the cylindrical tank wall), it was possible to determine the distribution of velocity that gave rise to local changes in water-surface elevation. This was more difficult than anticipated. One example has been worked out in detail – the observed crater shown in figure 8 as the solid line. The corresponding velocity field required to produce the observed crater is shown as the dotted line in figure 9. However, this result is not correct, since an estimate of the curvature of the surface shows that surface tension will have an important influence. The vortex strength was determined by first calculating the pressure difference made up by surface tension using the equilibrium curvature in the central region of the vortex. Then, the surface shape in the absence of surface tension was calculated by choosing as a model velocity distribution the Rankine vortex

$$\left.\begin{aligned} V &= (\omega_c + \Omega)r \quad (r \leqslant \epsilon), \\ V &= \frac{\Gamma}{2\pi r} + \Omega r \quad (r \geqslant \epsilon), \end{aligned}\right\} \tag{3.7}$$

where V is the absolute azimuthal velocity relative to the centre of the vortex, and ϵ, ω_c, and Γ are parameters to be determined (only two are independent since $\Gamma = 2\pi\epsilon^2\omega_c$). The circulation and vortex core radius were determined by choosing the best fit in the central portion of the vortex. The corrected velocity distribution is

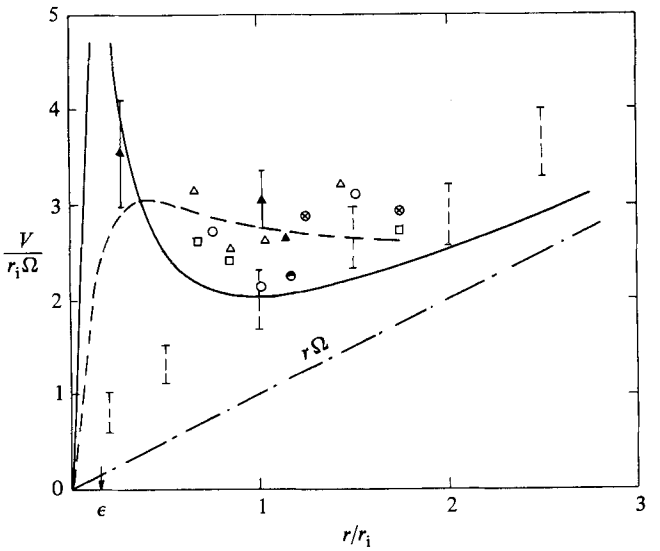

FIGURE 9. Radial velocity distribution in a vortex relative to a frame moving with the centre of the vortex for $Ro_g = 3{\cdot}32$: ----, velocity field corresponding to the observed crater in figure 8; ——, velocity field obtained from the vortex model including the effect of surface tension. The characteristic radius $r_i = (\Gamma/2\pi\Omega)^{\frac{1}{2}}$. The open symbols correspond to velocities determined from selected vortices in figure 2(*b*) and ▲ refers to velocities determined from ciné films. ⊤ indicates velocities measured by McEwan (1976).

shown as the solid line in figure 9, and the surface shape – if indeed there was no surface tension – is shown as the dotted line in figure 8. The correction to the velocity profile is dramatic, and indicates the essential need to include surface tension. The 'best-fit' values are

$$\epsilon \approx 1{\cdot}5 \text{ mm},$$
$$\omega_c \approx 248 \text{ rad s}^{-1},$$
$$\Gamma \approx 35 \text{ cm}^2 \text{ s}^{-1}.$$

The core size is thus slightly larger than the core indicated by the bubbles. The concentration of vorticity is considerable. The core rotation ω_c is about 40 times larger than the ambient rigid-body rotation. The circulation contained in one core is only about 0·20% of the circulation around the tank, however. Since there are approximately 20 such vortices (figure 4), the total circulation bound up in the vortex cores represents approximately 4·5% of the tank circulation.

The iteration scheme required to eliminate the effect of surface tension might suggest that the above values are particularly sensitive to the model chosen. In fact, this is not so. The value of ω_c depends primarily upon the difference in pressure made up by the surface tension at the centre of the core (i.e. the increased depth of the crater in figure 8). This in turn depends only upon equilibrium surface curvature at the centre, and the value of surface tension, both of which are known reasonably accurately. The same flow has also been photographed with a surface-tension-reducing agent added. Figure 10 shows the free surface for grid Rossby number equal to 3·32, with the surface-tension-reducing additive. The effect of the additive was to reduce surface tension to about half the value for water alone. In this case, surface craters are formed (figure 10), with indentations comparable to those estimated by our model.

The velocity distribution in figure 9 is non-dimensionalized by the radius r_i, which

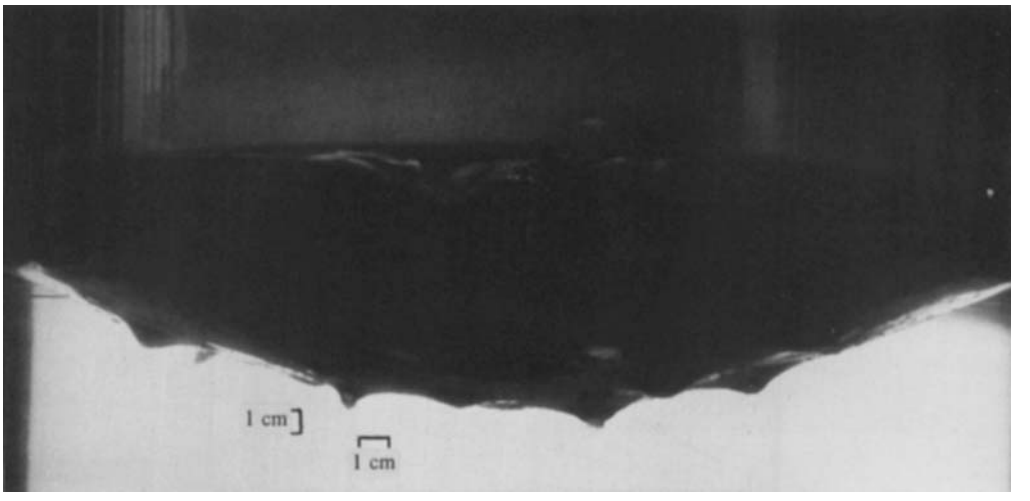

FIGURE 10. Photograph of the free-surface deformations caused by the vortices. Surface tension has been reduced by about 50%.

may be thought of as the characteristic radius for the vortex. It is the radius for which the model velocity in the rotating frame is equal to the rotational velocity of the reference frame. It is obtained by equating

$$r\Omega = \frac{\Gamma}{2\pi r},$$

to give

$$r_i = \left(\frac{\Gamma}{2\pi\Omega}\right)^{\frac{1}{2}} \approx 0{\cdot}94 \text{ cm} \tag{3.8}$$

for the present case. The induced velocity at $r = r_i$ in the rotating frame is 5·9 cm s^{-1}. Using this velocity and the length $2r_i$ gives a Rossby-number estimate for the active regions as $Ro = 0{\cdot}25$, which is essentially equal to Ro_T calculated in §3.3.

A direct measurement of core velocities is extremely difficult, as discussed in §3.1. Nevertheless, several data are shown in figure 9. The points indicated with open symbols were obtained by observing wood-particle streaks in a horizontal plane, giving images as shown in figure 2(*b*); and the points with solid symbols were obtained from observing more neutrally buoyant particles on a ciné film (frame by frame) with illumination in a vertical plane. We have, perhaps, slightly more confidence in the solid-symbol points because the individual particles can be identified unambiguously and followed through many time steps. The solid symbols were taken from particle paths directly under the free surface for the vortex that was used to determine the model velocity distribution. The open symbols were from other vortices, and need not agree in detail with the model.

One final interesting conclusion can be made regarding the distribution of velocity. We now have two expressions as estimates for the scale of the size of vortices in the rotation-dominated flow: the expression for $2r_i$ in (3.8), and the expression for l_T in (3.5*a*). Equating these two expressions gives an expression for the circulation Γ that is independent of rotation rate.

$$\Gamma \approx \frac{\pi}{4}\left(\frac{K_1 K_2}{Ro_T}\right)n$$

(K_1 has units of length^2). The reason for this interesting result is that as the size of

the vortices increases with increasing Ro_g (cf. (3.5)) vorticity is gathered from a larger region, and the circulation remains relatively constant. This result is born out directly by observations of the velocity field at the three grid Rossby numbers (figures 2*b*, 3*a*, *b*).

3.5. *Observations of travelling wave disturbances*

One of the most interesting dynamical aspects of this rotating turbulent flow are the wave disturbances which are observed to travel along the cores. Figure 7, for example, shows several waves travelling on a single core. The positions of the waves are indicated in the figure. The disturbances have the form of a helical distortion of the core (well-defined in figure 7 (*a*), but less so in 7 (*b*)). The distortions propagate as a result of self-induction. The waves are not the result of the presence of gas bubbles in the vortex cores, since similar wave motions are observed in the complete absence of bubbles. However, the wave motions are not so distinct when wood particles or dye are used as tracers.†

The possibility of such vortex core motions was discussed in general terms by Batchelor (1967), by Hasimoto (1972), and recently by Kida (1981). Simple dynamical arguments suggest four possible wave types. These possibilities are sketched in figure 11. In all cases the core vorticity vector is oriented downwards (clockwise rotation, as in the experiment). Example (*a*) is a left-handed open helix, which might for simplicity be called a 'left kink'. The induced motion causes the left kink to propagate upward in the *opposite direction* to the vorticity vector. The pattern rotates as it travels, with a sense of rotation *opposite* to the rotation of the core. A helix may also double back upon itself to form a loop or 'antikink'. Example (*b*) is a left antikink, which also travels in a direction *opposite* to the vorticity vector, but the pattern rotates in the *same* sense as the core rotation. From symmetry, the other two possibilities are a 'right kink', and a 'right antikink', both of which propagate in the same direction as the vorticity vector. Again, the right kink rotates in a sense opposite to the core rotation, while the right antikink rotates in the same sense as the core rotation (figures 11 *c*, *d*). All of these wave types have been observed in our rotating turbulent flow. Typical waves have wave envelopes that extend over several centimetres (wavelenths along core axis) and wave amplitudes of a fraction of a centimetre.

4. Vortex-filament solitons

The waves appear to propagate as single entities, and to travel many times their length without appreciable change in shape. This fact suggests the possibility of a solitary-wave (soliton) description for the phenomenon. Hasimoto (1972) has shown that helicoidal solitons can exist on a single isolated vortex core in an irrotational flow. In the model the circulation is assumed constant, and the vortex filament is not allowed to stretch. The induced motion is calculated as if the vortex filament were

† The gas bubbles are assumed to represent correctly the vortex axis, but they underestimate somewhat the vortex core diameter, as is seen from figure 8. Arguments in favor of a correct representation of the axis can be deduced from an examination of figure 7, which shows that the bubble core (bright) is centred in the vortex whose limits are indicated by the horizontal wood-particle streaks. The inertia of the bubbles was small and therefore they easily followed any core distortions. The buoyancy effect was negligible, since the bubbles were observed to rise only very slowly when turbulence was absent. Dye was also used to visualize the helicoidal distortions, but it was difficult to inject the dye into the vortex centre, and because of vortex breakdown, the dye would rapidly diffuse over a broader region.

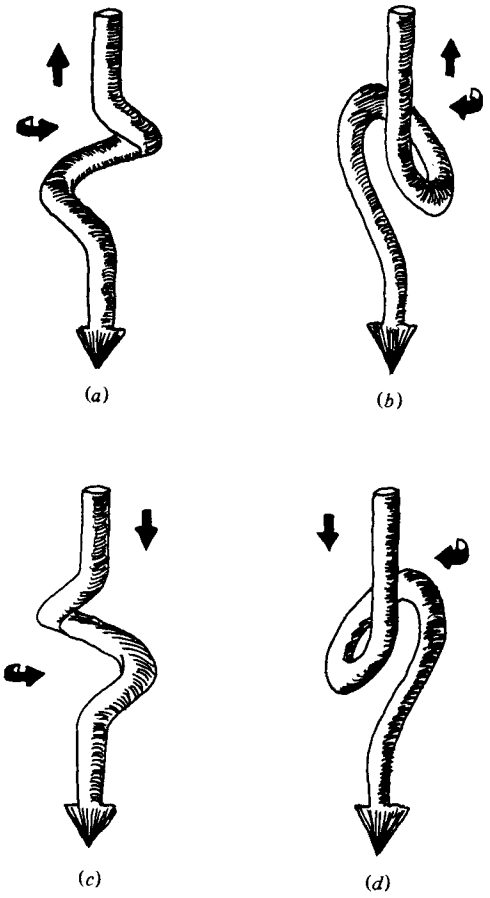

FIGURE 11. Schematic representation of possible wave shapes: (*a*) left kink; (*b*) left antikink; (*c*) right kink; (*d*) right antikink. Arrows indicate the direction of propagation/rotation of the wave patterns.

a circular ring having the same curvature as the actual filament. With these assumptions, Hasimoto demonstrated analytically that wave properties are governed by a nonlinear Schrödinger equation. For a vortex filament that is straight at infinity there is a particular solution giving a soliton of constant torsion and varying curvature (torsion is the rate of change of binormal direction along the filament).

The assumptions of the theory are not precisely appropriate to the present experiment. First, there are many vortex cores in our experiment, not just a single core. But although interactions between cores are certainly important, there are nonetheless intervals of time when individual cores are far from neighbours. Secondly, each vortex core is not an 'isolated vortex' surrounded by irrotational flow, but regions of highly concentrated vorticity in a rotational ambient fluid. As we have seen, however, the core regions have typical vorticities that are 40–50 times larger than the ambient vorticity and thus may qualify approximately as 'isolated vortices'. Finally, rotation is not included in the model. It will be shown *a posteriori* that the Rossby numbers associated with the wave-induced motions are moderately large. Rotation, then, is indirectly responsible for the regions of concentrated vorticity, but rotation has little direct effect on the wave motions themselves.

One particular case is chosen for detailed comparison. This wave is shown

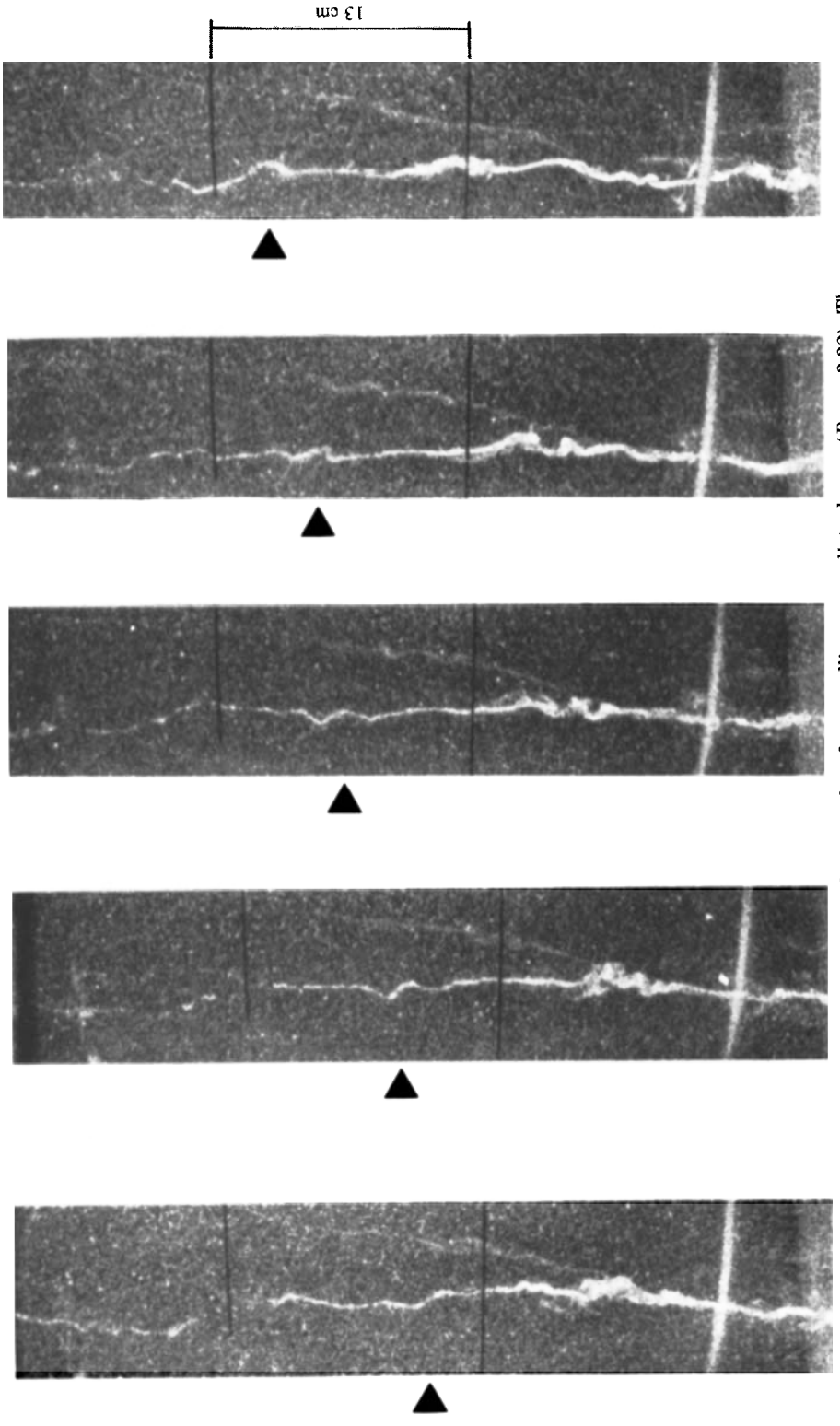

FIGURE 12. Time sequence photographs of a travelling wave disturbance ($Ro_g = 3{\cdot}32$). The mean position of the wave is marked by arrows.

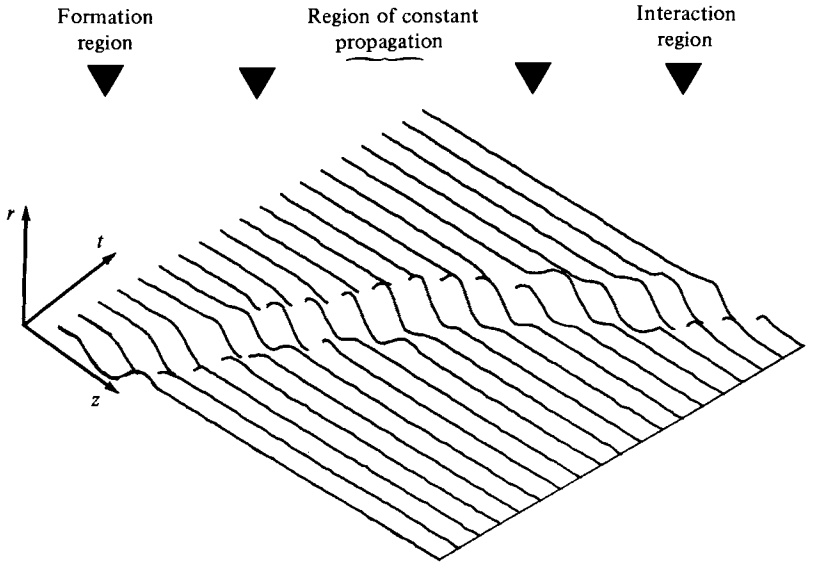

FIGURE 13. Computer trace of the solitary wave shown in figure 12. The vortex core beyond the wave disturbance has been straightened.

sequentially in figure 12. The core is relatively straight with few external disturbances. The wave is observed to form on the lower portion of the core and to travel upward with anticlockwise rotation – it is a left kink. The length of the wave is approximately 5 cm and the lateral excursion of the core is approximately 0·6 cm. This wave is somewhat longer than the average wave observed. (Most of the shorter waves are too ill-defined to allow comparison.)

The wave shape at successive times is traced from film, and the result digitized for computer manipulation. An isometric position–time history of the wave is shown in figure 13. (Irregularities on the core not associated with the wave have been suppressed.) A careful inspection of the sequence shows that the wave begins to move slowly; travels for a time at nearly constant speed; and finally accelerates and becomes entangled with another wave near the end of the trajectory. We have chosen to analyse the central constant-velocity portion of the record indicated in figure 13. During 10–12 camera frames the wave travels upward approximately one wavelength and rotates approximately one half-revolution.

Two simple comparisons with theory are possible. The first is the wave shape; and the second comparison is the ratio of the propagation speed of the envelope to the maximum rotation speed of the pattern. The theoretical wave shape predicted by Hasimoto is (with slightly different notation):

$$\nu x = \frac{2}{1+T^2}\operatorname{sech}\eta\cos\phi(\eta,t) \tag{4.1a}$$

$$\nu z = \nu s - \frac{2}{1+T^2}\tanh\eta + \nu z_0, \tag{4.1b}$$

$$\nu r_{\max} = \frac{2}{1+T^2}, \tag{4.1c}$$

$$\eta = \nu(s-ct), \tag{4.1d}$$

$$\phi(\eta,t) = T\eta + \omega_P t, \tag{4.1e}$$

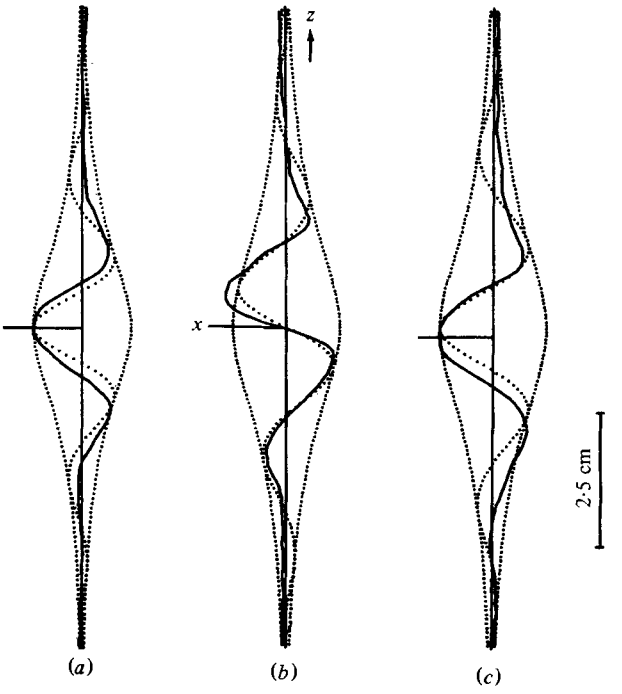

FIGURE 14. Comparison of the experimental wave and the constant-torsion soliton shape given by Hasimoto (1972): (*a*) $t = 0$; (*b*) t = one-quarter period; (*c*) t = one-half period. The lateral scale is stretched by a factor of two.

where z is the direction of the undistorted core, s is distance along the distorted filament, x is the lateral coordinate of the core, ϕ is the phase of the pattern, and ν is a scale parameter having dimensions of (length)$^{-1}$. The quantity $r_{\max}$ is the maximum lateral excursion of the filament independent of phase, and T is the shape parameter for the wave. According to theory, T is related to wave torsion and maximum wave curvature:

$$T = \frac{2 \times \text{wave torsion}}{\text{maximum wave curvature}}. \tag{4.2}$$

The wave shape depends only on T. In practice the scaling factor ν is first determined; then T is chosen to best fit the overall wave shape for three time instants corresponding to $\frac{1}{4}$ rotation of the pattern. Together these represent a time sequence of $\frac{1}{2}$ revolution of the wave. The result of the comparison is shown in figure 14. The best overall fit of the three shapes yields the values $T = 3{\cdot}125$ for $\nu = 0{\cdot}64$ cm^{-1} and $r_{\max} = 0{\cdot}29$ cm. The wave torsion and maximum curvature are then computed to be respectively 2·00 cm^{-1} and 1·28 cm^{-1}.

At $t = 0$ and π/ω_{P}, the theoretical envelope is slightly too short, and a value of $T = 3{\cdot}25$ would have been best. At $t = \pi/2\omega_{\mathrm{P}}$, the envelope is too long, and a value $T = 3{\cdot}00$ would have been best. Thus $T = 3{\cdot}125$ is a compromise. The other notable disparity is the behaviour farthest from the centre of the wave, where the theory predicts much more 'oscillation' than is observed. These oscillations are extremely small – less than one-tenth of a centimetre – and are probably below the resolution of our measurements. Overall the match is exceedingly good in our opinion.

The wave envelope travels upward with group velocity $c = 15{\cdot}7$ cm s$^{-1} \pm 10\,\%$, and

has a rotation rate $\omega_P = 13{\cdot}2$ rad s$^{-1} \pm 10\,\%$. Using the observed maximum radius $r_{max} = 0{\cdot}29$ cm, the ratio

$$\frac{\text{group velocity}}{\text{max pattern rotation speed}} = \frac{c}{\omega_P r_{max}} \approx 4{\cdot}05^{\pm 0{\cdot}7}, \tag{4.3}$$

with an estimated accuracy of $\pm 20\,\%$. The theoretical prediction is

$$\frac{|c|}{|\omega_P r_{max}|} = \frac{|T(T^2+1)|}{|-T^2+1|} = 3{\cdot}84. \tag{4.4}$$

This second, independent comparison also gives agreement.† A Rossby number for the wave can be defined in terms of the group velocity and the maximum wave radius:

$$Ro_w \approx \frac{c}{\Omega r_{max}} = O(5). \tag{4.5}$$

Under this circumstance, rotation would not be expected to affect the wave appreciably.

The tentative conclusion, based upon comparison between experiment and theory, is that *the isolated waves we observed are indeed solitons*; and are approximately described by the theory of Hasimoto. With this in mind, the theory can be used to draw several additional conclusions which are in qualitative accord with experimental observation. The theoretical prediction for the propagation speed is

$$c = 2\left[\frac{2T}{1+T^2}\frac{1}{r_{max}}\right]G. \tag{4.6}$$

The quantity in brackets is the wave torsion defined by Hasimoto – here given in terms of T and r_{max} – and G is the coefficient of local induction:

$$G = \frac{\Gamma}{4\pi}\ln\frac{L^*}{\epsilon}. \tag{4.7}$$

Again, Γ is the vortex circulation, and ϵ is the vortex-core radius. G is the leading term in the expansion to calculate induced motion, and is the only term kept in the induction approximation (cf. Batchelor 1967). The length L^* may be thought of as an equivalent interaction length, i.e. the effective length of core that must be included in the induction calculation. The effective length is not predicted, although L^*/ϵ should remain constant within the limit of the asymptotic theory. The wave properties just determined, together with the previously estimated value for the circulation Γ, allow a *rough* estimate of the constant $\ln(L^*/\epsilon)$,

$$\ln\frac{L^*}{\epsilon} \approx 1{\cdot}4, \tag{4.8}$$

and of L^*,

$$L^* \approx 4{\cdot}1\,\epsilon. \tag{4.9}$$

All solitons should approximately obey the relationship,

$$c \approx 0{\cdot}45\frac{T}{1+T^2}\frac{1}{r_{max}}\Gamma. \tag{4.10}$$

† There is a question concerning the proper interpretation of pattern rotation. The above expression ensures that the wave pattern having $T = 1$ does not rotate – a result that seems physically correct on the basis of symmetry. The solution of Hasimoto would give the ratio to be simply T; this result compares slightly less favourably with the experimental observation.

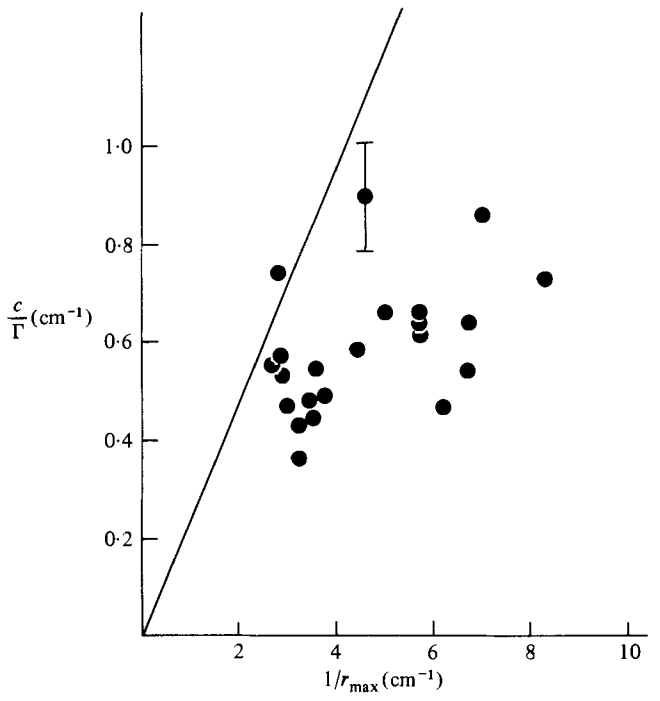

FIGURE 15. Observations of group velocity as a function of maximum wave amplitude (taken from film).

The propagation speed thus depends upon circulation Γ; maximum wave excursion, or amplitude, r_{max}; and wave shape characterized by the parameter T. The conclusion is that waves of fixed circulation and fixed amplitude (r_{max}) travel at different speeds depending upon wave shape. More surprising is the conclusion that waves of fixed circulation and fixed shape travel at a speed *inversely proportional* to wave amplitude. The reason is that wave-propagation speed is proportional to wave torsion (not to wave amplitude); and for fixed shape, a wave of smaller amplitude has the larger torsion. An approximate upper bound on the maximum propagation speed of disturbances on a core of fixed circulation is obtained by noting that the quantity $T/(1+T^2)$ has a maximum value equal to $\frac{1}{2}$ at the value $T = 1{\cdot}0$. The upper-bound estimate is

$$c \leqq \frac{0{\cdot}23\Gamma}{r_{max}}. \tag{4.11}$$

Measurements of wave speeds taken from films are shown in figure 15. The measured values are divided by the previously estimated value of circulation ($\Gamma = 35$ cm s^{-1}) and plotted against the inverse of the observed maximum wave radius r_{max} expressed in centimetres. There is an indication that smaller waves travel faster, but the data are far from conclusive. The upper bound (4.11) on wave speed does give a reasonable estimate for the larger waves, but is much too high for waves of smaller amplitude. Possibly, other effects intervene to limit the wave speeds of the smallest waves. Finally, it is interesting to note the relatively small range of wave amplitudes which were observed. The largest waves have a maximum radius (lateral displacement of centreline of core) of the order of 0·3–0·4 cm, while the smallest waves observed have radii of perhaps 0·1–0·12 cm. In terms of the previous estimate of core

radius $\epsilon \approx 0{\cdot}1$–$0{\cdot}20$ cm, the largest waves observed have $r_{\max} \approx (3$–$4)\epsilon$, and the smallest waves have $r_{\max} \approx \epsilon$.

5. Wave interaction: vortex-core breakdown

Typical vortex cores contain many propagating waves. For the case $Ro_g = 3{\cdot}32$ we have estimated the number of waves crossing (imaginary) horizontal planes per unit time. The results are

$$\text{number of upgoing waves/second} \approx \frac{1{\cdot}1\Omega}{2\pi}, \tag{5.1}$$

$$\text{number of downgoing waves/second} \approx \frac{0{\cdot}6\Omega}{2\pi}. \tag{5.2}$$

The results are independent of vertical position in the tank, provided that one is not too close to either boundary. From the results of §5 an average wave-propagation speed can be estimated as

$$\bar{c} \approx \frac{0{\cdot}12\Gamma}{\bar{r}_{\max}}. \tag{5.3}$$

An estimate for average wave spacing can be obtained by use of (5.1), (5.2) and (5.3):

$$\text{average spacing of upward travelling waves} \approx \frac{0{\cdot}69\Gamma}{\Omega \bar{r}_{\max}}, \tag{5.4a}$$

$$\text{average spacing of downward travelling waves} \approx \frac{1{\cdot}26\Gamma}{\Omega \bar{r}_{\max}}. \tag{5.4b}$$

Thus on our 45 cm vortex core there are, on average, 3–4 upgoing waves and 1–2 downgoing waves. Wave interactions are frequent and often dramatic. Because there is so much activity on the vortex core, it is extremely difficult to follow the details of individual interactions. The following conclusions about wave interactions are therefore somewhat sketchy and preliminary. Additional, controlled experiments on wave interaction are planned.

Generally speaking, wave interactions involve energy dissipation, small-scale turbulence production, and considerable local disruption of the vortex core region. There may be cases in which waves interact without subsequent modification of the core structure, but we were not able to demonstrate such interaction conclusively. We have attempted to classify the interactions leading to core breakdown into three categories; an example in each category is shown in figure 16 for $Ro_g = 3{\cdot}32$. The first category (figure 16*a*) is believed to be the result of reflection interaction between an upgoing and a downgoing wave. The second category (figure 16*b*) is believed to represent an overtaking interaction of two waves travelling in the same direction, but having different wave speeds. The third category, which produces the most violent disruption (figure 16*c*), appears to be caused by a single wave of large torsion and may not be an interaction at all. The wave amplitude grows substantially as the wave progresses, and we cannot, however, rule out the possibility of additional waves accumulating from behind.

The reflection interaction of two waves often produces a loop as seen in figure 16(*a*), (4)–(5). The spiral structure of one of the waves is squeezed and eventually folds over (4). The effect of the folding is a sudden reversal in the sense of rotation. Eventually, a loop forms (5)–(6), and the core ruptures in the vicinity of the loop (7)–(8). A 'patch' or 'spot' of small-scale turbulence develops, grows in size, and redistributes the core

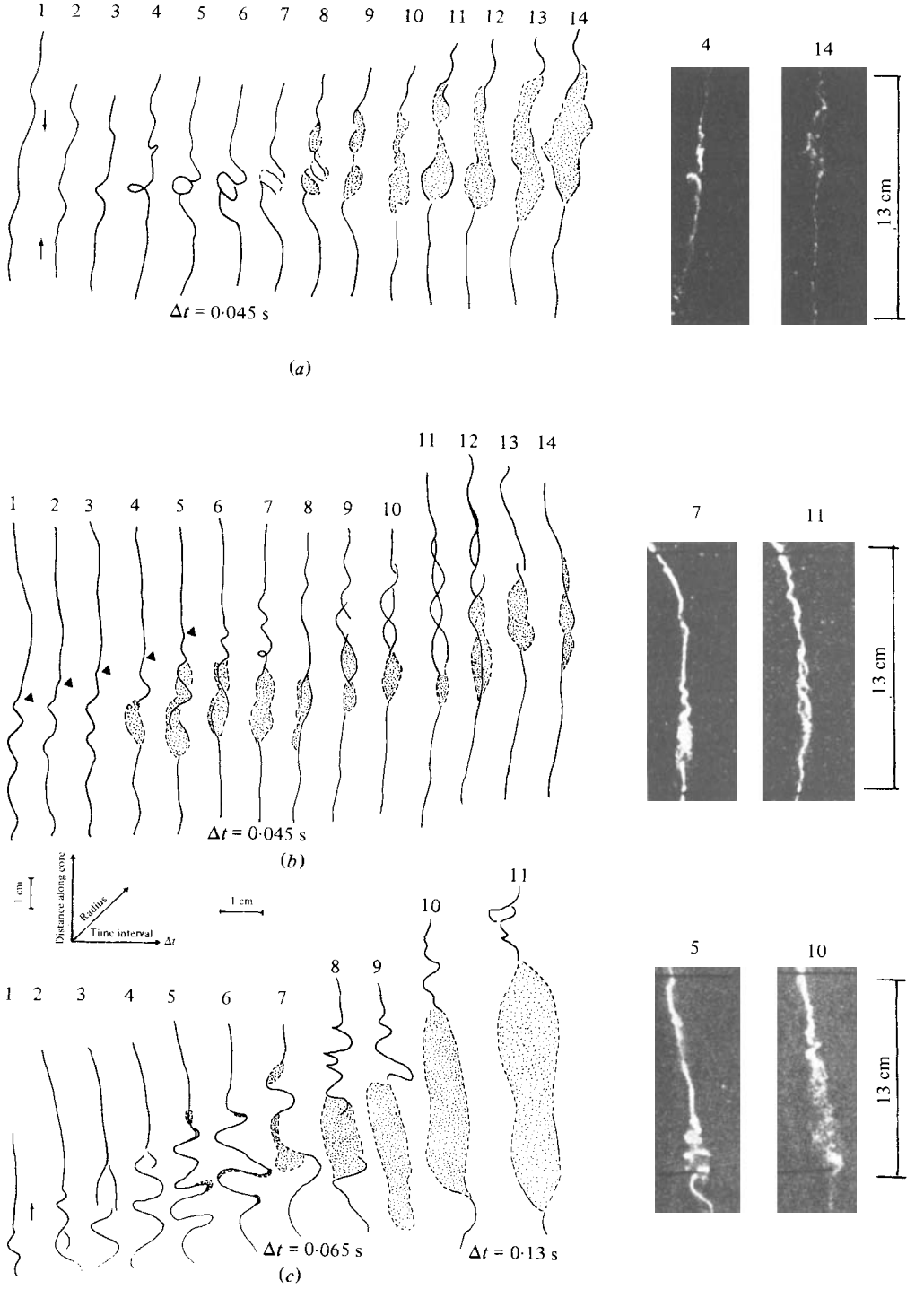

FIGURE 16. Most frequent local vortex-breakdown modes: (*a*) reflection-interaction (loop); (*b*) overtaking-interaction (double-stranded helix); (*c*) overtaking-interaction (spiral) mode. The vortex core is traced at regular time intervals throughout the breakdown process.

vorticity over a much broader region (8)–(14). The interaction region is almost stationary in the tank. The timescale of the breakdown (1)–(14) is of the order of one-half a rotation period π/Ω. In another half-rotation period, the turbulence spot dissipates and the core reforms. Often a wave leaves the upper end of the turbulent spot near the end of the interaction (11)–(14).

The distinguishing feature of overtaking-interaction breakdown is the formation of a double-stranded helical core in the breakdown region. In figure 16(*b*), (4), a small rupture of the core occurs, although this may not always happen. The double-strand helix appears later, perhaps as a result of the waves overrunning one another. There is a pronounced drift of the breakdown region in the direction of wave propagation. The interaction is less violent and the recovery of the core more rapid than in the reflection-interaction breakdown. By (14) the core has practically reformed, this is approximately one-half rotation period π/Ω. Again a wave disturbance appears to propagate away from the breakdown region (12)–(13).

In figure 16(*c*) a wave of large torsion is seen progressing upward. It grows in amplitude (1)–(5) and small isolated disruptions appear at intervals along the core. This is followed by a complete disruption of the core behind the advancing wave front (8)–(11). The large turbulent spot left behind may take on a flatter shape as time progresses. The timescale of the breakdown is again about half a rotation period, and the recovery period is of the order of one rotation period. Sometimes these waves traverse a considerable fraction of the depth of the tank, which can lead to obliteration of the entire vortex. This does not happen frequently, however.

One is struck by the similarity between the features described and the more conventional observations of vortex breakdown in various laminar rotating-flow apparatus. A double-stranded helical form analogous to 16(*b*) was first observed by Sarpkaya (1971) and by Faler & Leibovich (1977) to be a possible mode of stationary vortex breakdown; and the large-amplitude spiral breakdown (16*c*) has been identified to occur on delta wings by Lambourne & Bryer (1961). It is plausible to conclude that waves of the *type observed here* are also responsible for these stationary-breakdown phenomena. In the stationary breakdown, a strong axial flow counters the forward propagation of the wave(s), effectively bringing the process to rest.

We have found nothing comparable to the axisymmetric bubble observed on delta wings and, for example, by Faler & Leibovich (1977), and by Escudier & Zehnder (1982) in their remarkable visualizations. Our flow lacks the symmetry that might be expected to be necessary to produce the axisymmetric bubble. On the other hand, the case involving head on collision of two waves doesn't seem to fit any descriptions of observed stationary vortex breakdown either. It may be that stationary breakdowns in most other devices start with a relatively 'clean' upstream flow, and that wave disturbances in these cases are produced only at the downstream end.

We have remarked on the possibility of complete core destruction by means of strong high-torsion waves. It is also possible for vortex cores to be destroyed by interaction with neighbouring cores. Typically two neighbouring cores approach one another over part of their length. They intertwine and produce considerable disturbance, which redistributes the vorticity over a broader region, approximately the dimension shown in (11) of figure 16(*c*). The intertwining may then continue up to the core until vortex cores are obliterated. The events that destroy complete cores happen less frequently than 'local' breakdowns. We have observed individual cores for as long as 30 rotation periods, but the average life time is probably 10–20 rotation periods. The important point to note is that the vortices disappear by way of catastrophic events and not by gradual Ekman dissipation.

6. Concluding remarks

To summarize, we describe the major features of the turbulence in our rotating flow experiment. Near the grid, the Rossby number is large and the turbulence is relatively unaffected by rotation. Farther from the grid, fluctuation amplitudes decrease, turbulent scales increase, and rotation becomes more important. At a local Rossby number of about 0·20, there is an abrupt transition, which terminates the turbulent Ekman layer. Above the Ekman layer, the character of the turbulent flow changes completely. This flow consists of concentrated vortices, which extend throughout the depth of the flow (and tend to penetrate downward into the Ekman layer). The vortices wander about in a random fashion and individual vortices have lifetimes of 10–30 rotation periods. Individual vortices seem to be well modelled by assuming a concentrated core and an outer, irrotational flow (superimposed upon the background solid body rotation). At a grid Rossby number of about 3, the core vorticity is approximately 40 times larger than this background vorticity 2Ω. The horizontal scale of the vortices is the same as the local turbulence integral scale at the transition height, and increases with the square root of the grid Rossby number. The core size (region of constant concentrated vorticity) is typically a factor of 7 smaller, and probably also increases with the square root of the grid Rossby number. The spacing *between* cores is about 5 times larger than the vortex scale and can be expected to have the same dependence on grid Rossby number. A consequence of this vortex-shape invariance (which is supported qualitatively by direct observation over the range of grid Rossby numbers 3·0–33·0) is that the circulation around each vortex depends upon the intensity of forcing but not upon the rotation. Since all scales are increased at lower rotation rates (larger grid Rossby numbers) the flow is able to collect vorticity from a larger area, and thus maintain roughly constant vortex circulation (this observation has interesting implications concerning the dependence of the strength of a tornado on the intensity of forcing (Hopfinger & Browand 1981)). We have used the phrase rotation-dominated rather than quasi-geostrophic to describe this turbulent field. When a Rossby number is calculated with a typical value of the turbulent velocity (taken at transition) and the vortex spacing which is indicative of the largest possible eddies, a value of 4×10^{-2} is obtained. In a global sense the motion could thus be considered quasi-geostrophic. But, rotation produces a curious juxtaposition: relatively slow moving, low-Rossby-number columnar features which nonetheless have vortical cores dominated by ageostrophic motions.

The principle manifestation of this non-geostrophic motion are the vortex-core waves. Isolated, propagating waves seem to be well described by the vortex-soliton theory of Hasimoto (1972). To our knowledge this is the first observation of solitons in a rotating turbulent flow (or in any other turbulent flow). In the parameter range investigated, these waves are an important part of the turbulence process. Away from the top and bottom boundaries of the tank (measurements were made at 17 cm, 30 cm and 43 cm from the grid), the number of waves crossing an arbitrary horizontal plane is practically independent of vertical position, (5.1), (5.2), and the number of upward-travelling waves is about a factor of two larger than the downward-travelling waves. A consistent interpretation is that waves are produced and destroyed in the interior of the rotating turbulent region; and the *difference* in numbers travelling upward and downward – approximately 0·5 waves s^{-1} – represents the upward wave flux from the Ekman layer. We have also noticed that waves travelling upward are, on the average, larger in amplitude than waves travelling downward. Thus there is a net wave-energy flux upward from the Ekman layer. The magnitude of this

wave-energy contribution has not been determined quantitatively, but our qualitative observations suggest it is not negligible.

The interaction of vortex-core waves almost always leads to the production of smaller scales of motion, which contribute to dissipation within the tank. It may seem to be a contradition that individual solutions are described well by a solution of the nonlinear Schrödinger equation, and yet do not appear to have the property of perfect reflection. One possibility is that the two interacting waves, together, have an amplitude so great that local breaking almost always occurs. It is significant also to note that the dissipative regions produced by wave breaking are intermittent in both space and time.

A more intriguing proposition is that the waves may also be responsible, at least in part, for the maintenance of the concentrated vorticity field. The initial formation time of the vortices is relatively short. This time was determined experimentally by first establishing a condition of rigid-body rotation and then starting the grid motion. The measured time for the first observation of concentrated cores extending over the whole depth was approximately

$$\frac{T_f \Omega}{2\pi} \approx 6\text{–}7, \tag{6.1}$$

where T_f is the formation time. Vortices seem to appear throughout the cross-section of the tank on this timescale, originating apparently first near the grid and rapidly filling the whole depth. This timescale implies a wave mechanism. (Dickinson & Long (1982) give an additional argument for a wave mechanism based upon the velocity of the turbulent–non-turbulent front.).

Once formed, the vortices must be continually resupplied, for diffusion will act to decrease the concentrations of vorticity. For example, laminar diffusion – on a timescale $t_d = O(\epsilon^2/\nu)$ – would significantly redistribute core vorticity in a time of several rotation periods. The vortices have lifetimes much longer than several rotation periods, and disappear by catastrophic breaking events – not by diffusion. Vortices can be maintained in the required equilibrium condition only by the presence of a time-averaged horizontal motion directed towards the core regions. The horizontal convergence could be supplied by a slow steady motion from a local region of scale l_T. The balance is sketched in figure 17 (*a*), and was discussed many years ago by Burgers (1948) in a slightly different context.

Conversely, the maintenance of vortex strength can be viewed as arising from the vertical stretching of the core, which is related by continuity to the horizontal convergence. The induced axial velocity associated with a propagating soliton is capable of transporting core fluid along the axis of the vortex. (The axial movement of individual particles has been observed qualitatively, but not with sufficient accuracy to compare with theoretical estimates.) In the steady state a portion of the energy to maintain the turbulence comes from the region near the grid (in the form of an excess of upgoing waves), but waves are also produced all along the length of the vortex cores. The local distortion of a vortex core by a neighbouring core might be expected to initiate a wave pair, one wave travelling upward and one downward. A local horizontal convergence would then be produced as a result of the wave motion (and the axial flow), as sketched in figure 17 (*b*). Unfortunately, we could not establish an unequivocal connection between vorticity concentration and wave motion. The present evidence is only suggestive, and other mechanisms providing the required horizontal convergence are possible. The true dynamical importance of the waves – as well as how the results might apply to oceanic and atmospheric phenomena – are subjects for future study.

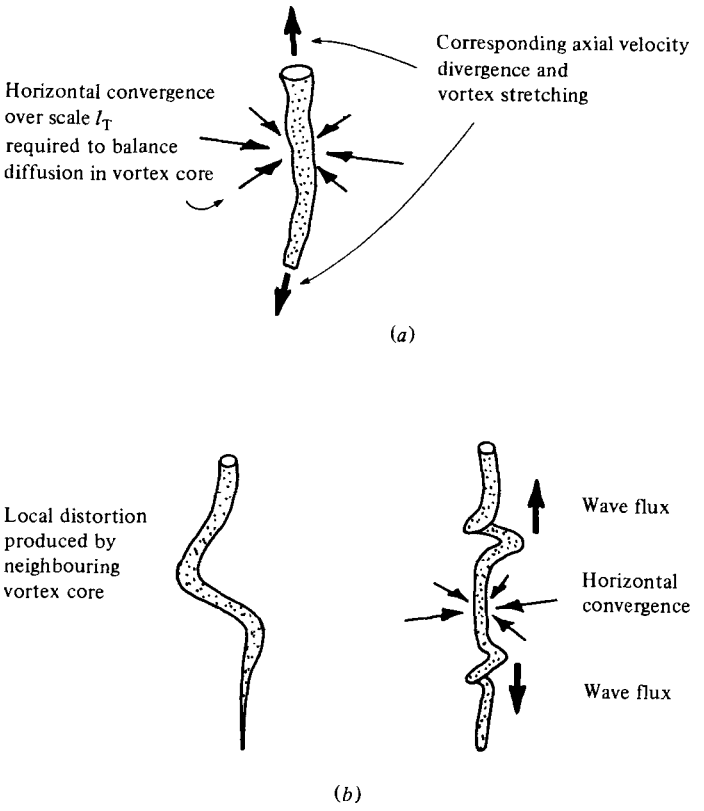

FIGURE 17. (*a*) Horizontal convergence required for maintenance of concentrated vorticity field. (*b*) Convergence produced by wave pair at a distortion of the vortex core.

The authors gratefully acknowledge helpful discussions with U. Frisch, P.-L. Sulem and J.-D. Fournier. Frisch and Sulem pointed out to us the possible relevance of the paper by Hasimoto to the observed wave phenomena. We thank Serge Layat for assistance in conducting the experiments. The research was partially financed by the Centre National pour l'Exploitation des Oceans under contract n 80/2345. One of the authors (F.K.B.) acknowledges support from ONR under contract number N00014-82-K-0084 during the final stages of the work.

REFERENCES

BATCHELOR, G. K. 1967 *An Introduction to Fluid Dynamics*. Cambridge University Press.

BRETHERTON, F. P. & TURNER, J. S. 1968 On the mixing of angular momentum in a stirred rotating fluid. *J. Fluid Mech.* **32**, 449–464.

BURGERS, J. M. 1948 A mathematical model illustrating the theory of turbulence. *Adv. Appl. Mech.* **1**, 171–199.

COLIN DE VERDIERE, A. 1980 Quasi-geostrophic turbulence in a rotating homogeneous fluid. *Geophys. Astrophys. Fluid Dyn.* **15**, 213–251.

DICKINSON, S. C. & LONG, R. R. 1982 Oscillating grid turbulence including effects of rotation. Submitted to *J. Fluid Mech.* (in the press).

ESCUDIER, M. P. 1979 Estimation of pressure loss in ring-type exit chambers. *Trans. A.S.M.E.* I: *J. Fluids Engng* **101**, 511–516.

ESCUDIER, M. P., BORNSTEIN, J. & MAXWORTHY, T. 1982 The dynamics of confined vortices. *Proc. R. Soc. Lond.* **383**, 335–360.

ESCUDIER, M. P. & ZEHNDER, N. 1982 Vortex-flow regimes. *J. Fluid Mech.* **115**, 105–121.

FALER, J. & LEIBOVICH, S. 1977 Disrupted states of vortex flow and vortex breakdown. *Phys. Fluids* **20**, 1385–1400.

GOUGH, D. O. & LYNDEN-BELL, D. 1968 Vorticity expulsion by turbulence: astrophysical implications of an Alka-Seltzer experiment. *J. Fluid Mech.* **32**, 437–447.

HASIMOTO, H. 1972 A soliton on a vortex filament. *J. Fluid Mech.* **51**, p. 477–485.

HOPFINGER, E. J. & BROWAND, F. K. 1981 Intense vortex generation by turbulence in a rotating fluid. In *Proc. IUTAM–IUGG Symp. on Concentrated Atmospheric Vortices, Reading.*

HOPFINGER, E. J. & BROWAND, F. K. 1982 Vortex solitary waves in a rotating, turbulent flow. *Nature* **295**, 393–396.

HOPFINGER, E. J. & TOLY, A.-J. 1976 Spatially decaying turbulence and its relation to mixing across density interfaces. *J. Fluid Mech.* **78**, 155–175.

IBBETSON, A. & TRITTON, D. Y. 1975 Experiments on turbulence in a rotating fluid. *J. Fluid Mech.* **68**, 639–672.

KIDA, S. 1981 A vortex filament moving without change of form. *J. Fluid Mech.* **112**, 397–409.

LAMBOURNE, N. C. & BRYER, D. W. 1961 The bursting of leading-edge vortices: some observations and discussion of the phenomenon, *Aero. Res. Counc. R.* no. 3282.

MCEWAN, A. D. 1976 Angular momentum diffusion and the initiation of cyclones. *Nature* **260**, 126–128.

SARPKAYA, T. 1971 On stationary and travelling vortex breakdowns. *J. Fluid Mech.* **45**, 545–559.

SCORER, R. S. 1966 Origin of cyclones. *Sci. J.* **2**, 46–52.